High-Resolution Remote-Sensing Image Registration Based on Angle Matching of Edge Point Features

Qing Guo ⬮ , *Member, IEEE*, Mengmeng He, and An Li

Abstract—Remote-sensing image registration is an important prerequisite for many remote-sensing applications. The accuracy, efficiency, and automatic degree of registration have direct impacts on follow-up applications. With the improving of remote-sensing resolution, the size and the data amount of remote-sensing image are constantly increasing. Meanwhile, with the development of remote-sensing application, the performance of registration is also put forward increasing requirement. Therefore, this paper proposes an automatic and fast image registration method based on the angle matching of edge point features (EPFs). First, the original image is transformed by the Haar wavelet to get the approximate image to improve the registration speed. Second, edges in different source images are extracted by different edge detectors. Then, edge line features are transformed into EPFs to get accurate positioning and stable features. Third, the initial matching point pairs (MPPs) are determined by the ratio—the minimum angle to the second minimum angle between feature vectors of EPFs—which is less than a threshold. Fourth, in order to enhance the registration accuracy, the random sample consensus is improved by adding the quality constraint condition to delete error MPPs. Finally, the block thought is used to uniformly choose MPPs to calculate the affine transform parameters, which avoids the local optimal problem and further improves the registration accuracy. Multiple high-resolution remote-sensing datasets of registration experimental results indicate that the proposed method is fast implemented and has high accuracy and effectiveness in processing efficiency.

Index Terms—Feature extraction, feature matching, high-resolution remote-sensing image automatic registration, image matching, image registration.

I. INTRODUCTION

IMAGE registration is a vital process which matches the same area images with the same or different sensors, the same or different time, and the same or different viewing angles to obtain the registered image with geometric consistency as the reference image.

Remote-sensing image registration is a basis in many remote-sensing information extraction and processing technologies, which is also the foundation of remote-sensing image analysis and application. At present, remote-sensing image registration is widely used in multisensor image fusion, image mosaic, target recognition, change detection, three-dimensional (3-D) reconstruction, remote-sensing quantitative information analysis, etc. Moreover, many theories and applications are under the assumed premise that the registration has been done well. Hence, the accuracy and the efficiency of image registration directly affect the follow-up applications.

The existing remote-sensing image registration methods are mainly divided into two categories: gray-based and feature-based [1], [2]. The feature-based methods do not directly use the gray values, but mainly rely on the salient features within a pair of images (a reference image and a sensed image). Compared with the gray-based method, the feature-based method is more slightly affected by noise. The latter method also has smaller amount of computation, stronger stability, and wider adaptability. Therefore, feature-based method is more suitable for the registration between remote-sensing images [3]–[5].

Feature-based registration methods are often based on point features [6], [7], line features [8], [9], as well as region features [10]–[12]. The positioning of point feature is accurate. The coordinates of matched point features can be directly used to calculate the space transformation relationship between the reference image and the sensed image. For the line feature (also called edge feature), it is stable. But the incomplete and broken line feature is easy to be produced. Region feature contains much useful information. However, it is not readily available. Therefore, the using of edge point feature (EPF) to carry out remote-sensing image registration not only can get accurate positioning, but also can obtain stable feature.

In addition, since the large amount of remote-sensing data has a wide range of applications, it is of great significance to automatically achieve the remote-sensing image registration and improve the efficiency of registration [13], [14]. Currently, the commonly used automatic registration methods based on point feature are the scale invariant feature transform (SIFT) [13], [15] and the speed up robust features (SURF) [16]. SIFT was first presented in 1999 [17] and was improved in 2004 [18]. This method translates the matching of images into the

This article has been accepted for inclusion in a future issue of this journal. Content is final as presented, with the exception of pagination.

2   IEEE JOURNAL OF SELECTED TOPICS IN APPLIED EARTH OBSERVATIONS AND REMOTE SENSING

matching of point features in multiscale space. SIFT achieves the advantages of scale invariance, high robustness in noise interference, and affine transform. But there is a large burden on the calculation. Moreover, the Euclidean distance is adopted to match feature points, which easily produces false matching point pairs (MPPs) and reduces the efficiency of image matching. The principal component analysis SIFT (PCA-SIFT) algorithm [6] simplifies the description of SIFT and improves the speed, but the matching accuracy is not as good as SIFT. Combining the weighted color model, SIFT is applied to do the stereo image registration [19]. The SURF [20] algorithm introduces an integral image that preserves the invariance of SIFT in the scale transform and optimizes the registration time. However, SURF has disadvantages in the low number of feature points, lower number of MPPs, and low matching ratio.

With the improvement of remote-sensing image resolution, remote-sensing image registration research has gradually shifted from low resolution to high resolution [21], [22]. However, since the high-resolution remote-sensing image has richer information, more complex details and textures, it is much more difficult to be registered than the medium-low resolution remote-sensing images, especially for submeter high-resolution remote-sensing images. Therefore, this paper presents a fast and automatic registration method based on the angle matching of EPFs for high-resolution remote-sensing images with rich detailed and textural information, in order to improve the registration accuracy and the computational efficiency.

This proposed method mainly includes the following five aspects.

1) Both the reference image and the sensed image are performed by the Haar wavelet transform to get the approximate images while preserving the main spatial structures of images. Then the registration of the original image is completed according to the matching result of the approximate image. Thus the amount of calculation is effectively reduced and the registration speed is improved.

2) According to different characteristics of different remote-sensing images, different edge feature detectors are used. For optical images, the canny algorithm [23] is used. For SAR images, the ratio of averages (ROA) algorithm [24] is used to extract the edge feature. ROA detector is a ratio edge detector which is defined as the ROA of pixel values between two nonoverlapping neighborhoods on opposite sides of the point. Moreover, the ROA detector considers the edge directions and the characteristic of speckle noise in SAR image. Then, edge line features are transformed into EPFs.

3) The feature vector of one EPF in the reference image is performed by the inner product with the feature vector of each EPF in the sensed image to calculate the angle. The initial MPPs are determined through the angle ratio—the minimum angle to the second minimum angle—less than a certain threshold. When all the feature points in the reference image are traversed, the total initial MPPs are obtained.
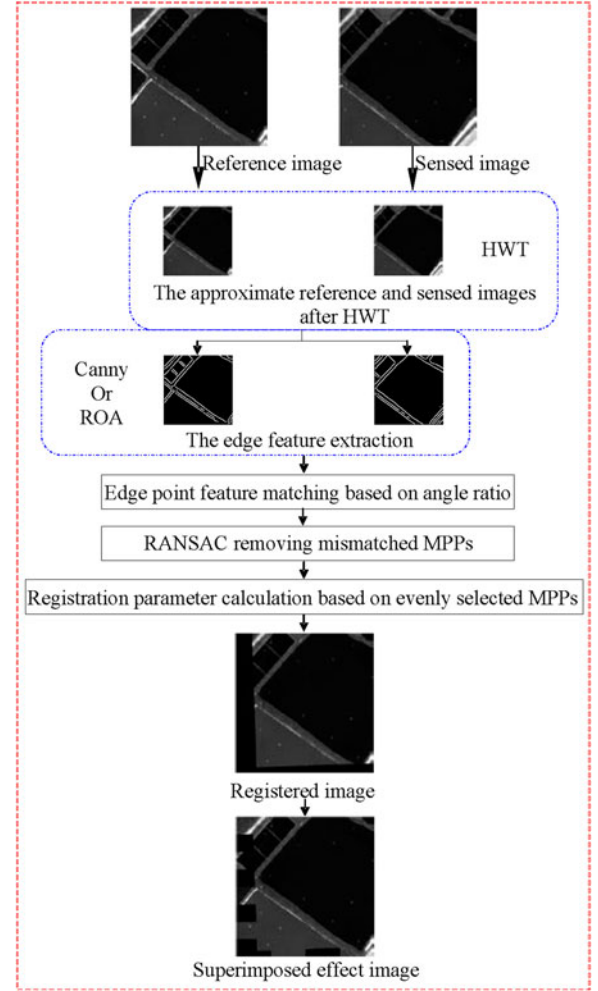

Fig. 1.   Flowchart of the image registration.

4) The variation on the random sample consensus (RANSAC) is proposed to filter the error MPPs, so as to increase the filtration speed and the registration accuracy.

5) Combining with the block idea, the MPPs are evenly selected to calculate the affine transform parameters, which further improve the registration accuracy.

II. PROPOSED METHOD

The proposed image registration based on the angle matching of edge point feature method (AMEPF) in this paper includes five steps: the Haar wavelet transform (HWT), the edge feature extraction, the EPF matching, the mismatched MPPs filtering, and the affine transform parameter calculation. The detailed flowchart of high-resolution remote-sensing image registration method is shown in Fig. 1.

In order to reduce the influence of speckle noise in SAR image, the filtering preprocessing is implemented by using the enhanced Frost filter before the HWT. The enhanced Frost filter determines different weight values for each pixel according to the variance of pixels, the gray mean of pixels, and the relative standard deviation of noise in the filter window. In other words,

This article has been accepted for inclusion in a future issue of this journal. Content is final as presented, with the exception of pagination.

GUO *et al.*: HIGH-RESOLUTION REMOTE-SENSING IMAGE REGISTRATION BASED ON ANGLE MATCHING OF EDGE POINT FEATURES 3
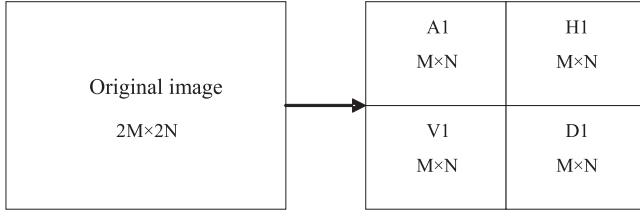

Fig. 2. One-level decomposition of the HWT.

different weight values are set for different pixels to adaptively smooth out the speckle noise. The speckle noise is effectively suppressed and the edge detail information is preserved by adjusting the filter weight according to the characteristics of the filter window.

A. Haar Wavelet Transform

In the previous image registration, most methods directly perform feature extraction after reading the image. However, with the remote-sensing image resolution getting higher and higher, the image size is also larger and larger. The direct feature extracting from the original image increases the calculation amount and reduces the image registration efficiency. The wavelet transform has the multiscale analysis ability which divides the image into one low-frequency approximate image retaining the main spatial structure and three high-frequency detailed information images. The HWT is widely used because of its simple orthogonal wavelet transform function. Hence, in this paper, before the feature extraction, the HWT is applied to get the approximation image with smaller size than the original image. Then, the registration is performed based on the approximation image.

The using of the approximate image after HWT did result in some information losing, but still retains the main spatial structure information which is sufficient for edge detection to ensure the registration accuracy. Moreover, the number of pixels in the approximate image (one-level HWT) is only one-fourth pixels of the original image, which improves the registration speed much. Theoretically, the speed can be improved four times. This is very important for high-resolution remote-sensing image registration with very large image size.

Fig. 2 shows the decomposition diagram of one-level HWT. After the HWT decomposition, the image is transformed to four images, which are the approximate image (A1), the horizontal detail image (H1), the vertical detail image (V1), and the diagonal detail image (D1). Herein, $2M \times 2N$ is the size of the original image and $M \times N$ is the size of small images after HWT.

B. Edge Feature Extraction

The common image edge extraction operators include Canny, Roberts, Sobel, and Prewitt [25]. These operators have good adaptability to optical images with additive noises. The Roberts operator normally extracts obvious discontinuous edges and partial edges. The Sobel and Prewitt operators are not good at detecting weak edges, which often leads to incomplete edges. The Canny operator not only can control the details of edges, but
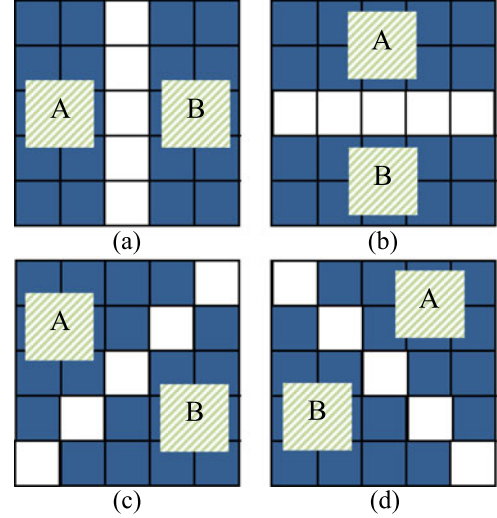

Fig. 3. Four detection directions of ROA. (a) Vertical direction. (b) Horizontal direction. (c) Diagonal direction of 45°. (d) Diagonal direction of 135° (the 5 × 5 window as example).

also can suppress the noises. Meanwhile, the Canny operator uses two thresholds to detect the strong edges and weak edges, which can detect the real weak edges well.

However, for the SAR image with strong multiplicative speckle noise, the above operators are not suitable. The ROA operator has a good inhibitory effect on the multiplicative noise, which can maintain the stability of edge detection and is suitable for the SAR image edge detection.

Therefore, based on the different characteristics of different images, this paper chooses Canny operator for optical image and ROA operator for SAR image as far as possible to extract the perfect edge line features, respectively. Edges are often associated with the boundaries of objects, which maintain the important structure property of an image. Then, the edge line feature is transformed into the EPF. EPFs combine the advantages of point features and line features. So, the use of EPF not only gets accurate positioning but also obtains stable features. Since the Canny operator is familiar, only the ROA operator is described.

For the ROA edge extraction operator, the ratio of the pixel gray mean values between two adjacent regions is used as the detection characteristic [24]. For SAR images, the center pixel point of a sliding window with a certain size is set as the point to be detected, then the sliding window is divided into A and B two regions by a straight line through that point. The gray mean values μ_A and μ_B of all the points in the two regions are calculated, respectively. Then, the maximum ratio value of the gray mean in two regions is as follows:

$$r_i = \max \left\{ \frac{\mu_A}{\mu_B}, \frac{\mu_B}{\mu_A} \right\}. \tag{1}$$

Herein, $r_i \geq 1$ ($i = 1, 2, 3, 4$ represent four edge directions in Fig. 3, respectively).

The closer to 1 r_i is, the nearer the mean values of A and B regions are. Then, the more likely A and B belong to the same region, the less likely the point is to be on the boundary between

A and B regions. Conversely, the larger r_i is, the greater the difference between A and B is, thus, the greater the likelihood which the point is on the boundary is. Because edge directions are different, each direction of four edge directions (as shown in Fig. 3) is detected once, then the ROA gradient strength r is the maximum value, that is $r = \max(r_1, r_2, r_3, r_4)$.

Since the r value is only related to the ratio of the gray mean value in the two regions, instead of depending on the specific gray mean value, a global threshold T is selected for comparison with the r value. When the r value is greater than the T value, the point is considered as the edge point.

C. EPF Matching

After the edge feature extraction, the binary images of the approximate reference and sensed images are obtained, respectively. According to the attribute of the edge binary image, the EPF information is extracted as the initial matching feature point set.

Before matching, the direction and description of the EPF need to be determined. Based on the idea of SIFT algorithm, this paper proposes an angle-based EPF matching algorithm.

1) First, the directional parameter of each EPF is specified using the gradient direction distribution characteristic of the neighborhood pixels around the EPF to make the matching operator with the rotation invariance.

2) For each approximate image $I(x, y)$, the gradient amplitude value $m(x, y)$ and the gradient direction $\beta(x, y)$ are computed by (2) and (3) in the 3×3 neighborhood window centered on the EPF

$$
m(x, y) = \\
\sqrt{\left[I(x+1, y) - I(x-1, y)\right]^2 + \left[I(x, y+1) - I(x, y-1)\right]^2} \tag{2}
$$

$$
\beta(x, y) = \tan^{-1} \frac{I(x, y+1) - I(x, y-1)}{I(x+1, y) - I(x-1, y)}. \tag{3}
$$

3) In the local gradients, the gradient direction range $[0, 2\pi]$ is divided into 36 segments. Each segment represents a gradient direction. Then, the gradient amplitude in each gradient direction is added up. In this gradient direction histogram, the peak cumulative value of the gradient amplitude represents the main direction of the EPF. When the cumulative value of the gradient amplitude in certain direction reaches above 80% of the peak, this direction is taken as the auxiliary direction of the EPF. Thus, one EPF may have multiple directions, which enhances the robustness of the image matching.

4) For any EPF, in order to ensure the rotation invariance of the feature vector, the x-coordinate axis direction of the 16×16 neighborhood, which takes the EPF as the center, is rotated to the main direction of the EPF. Then, the 16×16 neighborhood is divided into 4×4 subregions. In each subregion, the gradient histograms with eight directions are calculated. Then, the vectors for eight directions are generated. Thus, the 128-dimension (4*4*8)

feature vector is formed. For each EPF, there is a 128-dimension feature vector. The length of the feature vector is normalized, which is the feature descriptor of the EPF.

5) Finally, the EPFs are matched by calculating the angles between the feature vectors of EPFs. The angle value θ is obtained by performing (4) between the feature vector of each EPF in the approximate reference image (ARI) (the reference image is approximated by the HWT) and the feature vector of each EPF in the approximate sensed image (ASI) (the sensed image is approximated by the HWT). For one EPF in ARI, its feature vector with all the feature vectors of EPFs in ASI is calculated the angle, respectively. When the ratio of the minimum angle value $\theta_{\min}$ to the second minimum angle value $\theta_{\sec}$ is smaller than a certain threshold value t, such as (5), the two EPFs are considered as a pair of the MPP (matching point pair). This process is done until all the EPFs in ARI have been calculated

$$
\cos \theta = \frac{\vec{a} \bullet \vec{b}}{|\vec{a}| \times \left|\vec{b}\right|} \tag{4}
$$

$$
\frac{\theta_{\min}}{\theta_{\sec}} < t. \tag{5}
$$

Herein, $\vec{a}$ is the feature vector of EPF in ARI, and $\vec{b}$ is the feature vector of EPF in ASI.

D. Variation RANSAC Filtering Error MPPs

The RANSAC [26] algorithm is a random parameter estimation method to filter the error MPPs. There are the following five main specific steps.

1) Eight MPPs are selected randomly as the initial samples from the initial MPP set to compute a fitting model and the corresponding model parameters [27].

2) The initial MPP set is checked using the fitting model. Then, all interior points satisfying the threshold value of the model are found.

3) The numbers of interior points obtained from the fitting mode are counted.

4) Steps 1) to 3) are repeated until the obtained consensus set in certain iteration has enough interior points. Each time produces either a model which is rejected because of too few interior points, or a refined model with a consensus set size. In the latter case, the refined model is kept when the interior points are larger than the previously saved model.

5) The consensus set with relatively most interior point number is outputted, which is the final MPP set after the RANSAC filtering.

Although the RANSAC method can do robust estimation to filter out error MPPs with large errors, it needs repeated iterations and does not consider the quality of MPPs. In each iteration, the RANSAC method randomly selects any eight MPPs as the initial sample. Moreover, when the number of iterations is limited, the result may not be optimal. The error of image registration will be caused when a significant number of error MPPs

This article has been accepted for inclusion in a future issue of this journal. Content is final as presented, with the exception of pagination.

GUO *et al.*: HIGH-RESOLUTION REMOTE-SENSING IMAGE REGISTRATION BASED ON ANGLE MATCHING OF EDGE POINT FEATURES　　5

are present in the initial MPPs or a large number of mismatched point pairs are randomly selected as the initial samples.

Therefore, a variation on RANSAC by adding the quality constraint is proposed to remove error MPPs in the paper. As in the feature matching, the angle ratio—the minimum angle $\theta_{\min}$ to the second minimum angle $\theta_{\sec}$—is used as the quantitative representation of the quality of MPPs. The smaller the ratio is, the better the quality is. Specifically, the angle ratios of the initial MPPs are sorted from small to large. The first eight MPPs with the lowest ratio are selected as samples to compute the fitting model and the corresponding parameters. The model and parameters are fitted no longer by randomly selecting the initial samples but by the quality sorting of first eight MPPs. The above-mentioned variation solves the time consuming problem of multiple choosing sample sets, and effectively reduces the registration error caused by selecting error MPPs. Thus, the variation RANSAC improves the accuracy of image registration.

The main steps of the variation RANSAC to filter MPPs are as follows.
1) The initial MPPs are sorted by the angle ratio in ascending order. The first eight MPPs are selected as initial samples.
2) The fitting model and corresponding parameters are fitted using the selected initial samples that conformed to these data.
3) The fitting model is used to check all the other points in the MPPs. When the distance from this point to the model is less than a certain threshold, this point belongs to the inner point (conform to the model). Otherwise, this point is the outer point. Finally, the final MPP set is obtained.

E. Affine Transform Parameter Calculation

After the final MPPs with high quality are obtained by the variation RANSAC, the affine transform parameters are often computed in traditional methods by randomly choosing three MPPs. Because the selected MPPs may be concentrated in a certain area of the image, the parameters calculated are easy to get into the local optimum, which affects the image registration accuracy.

Therefore, a two-threshold method is proposed for the above-mentioned problem, in this paper, to evenly select MPPs. First, according to the coordinate values of final MPPs, the two-threshold method is used to divide blocks. When the row and column coordinate values of the MPPs are lower than the low threshold value, the MPPs belong to the first block. When the row and column coordinate values of the MPPs are higher than the high threshold value, the MPPs belong to the second block. The remaining MPPs are considered as the third block. The one-third of the row and column coordinate values of MPPs is the low threshold. The two-third of the row and column coordinate values of MPPs is the high threshold. Then, in each block, according to the quality of MPPs, the MPP with the best quality is adopted. Finally, the selected three MPPs are uniformly distributed in the image.

In addition, the size of the approximate image is half of the original size, because the one-level HWT decomposition is performed in this paper. Since these MPPs are obtained from the

approximate images, the coordinates of these MPPs are multiplied by 2 before calculating the affine transform parameters to get the parameters of the original image.

Specifically, the selected MPPs are formulated into the affine transform equation in the following:

$$\begin{pmatrix} x_n \\ y_n \end{pmatrix} = s \cdot \begin{pmatrix} \cos\alpha & -\sin\alpha \\ \sin\alpha & \cos\alpha \end{pmatrix} \cdot \begin{pmatrix} x_m \\ y_m \end{pmatrix} + \begin{pmatrix} d_x \\ d_y \end{pmatrix}. \quad (6)$$

Herein, s represents the scale, d_x and d_y represent the translation in the x and y directions, respectively, α represents the rotation angle, (x_n, y_n) and (x_m, y_m) are the coordinates of MPPs in the sensed image and the reference image, respectively. Then, the parameters of the affine transform are obtained by solving (6). Finally, the registered image is achieved from the original sensed image by the bilinear interpolation using the obtained affine transform parameters to complete registration.

III. EXPERIMENT AND RESULT ANALYSIS

In order to verify the efficiency of the proposed AMEPF method, experiments are carried out in five different situations: the same sensor optical image registration, the same sensor SAR image registration, image registration of different bands, image registration of different resolutions, and image registration of different temporal sensors.

For the experimental data, WorldView-2 (WV-2), Pleiades, and TerraSAR remote-sensing images are used. The detailed information is given in Table I. Moreover, in order to further prove the generality and applicability of this proposed method, the image size of the first four experiments is 512×512 and that of the fifth experiment is 2000×2800.

To validate the effectiveness of the proposed registration method based on AMEPF, manual registration and two typical automatic image registration methods based on SIFT and SURF are used for comparison. For manual registration, control point pairs are selected manually evenly over the reference and sensed images, and the polynomial affine transformation model is applied to achieve the image registration. The registration methods based on SIFT and SURF use the original RANSAC to filter error MPPs. The proposed method uses the variation RANSAC by adding the quality constraint. During the affine transform parameter calculation, the SIFT-based and SURF-based registration methods randomly select three MPPs. But, our proposed method evenly selects three MPPs in blocks by two-threshold way. The same bilinear interpolation is performed to get the

This article has been accepted for inclusion in a future issue of this journal. Content is final as presented, with the exception of pagination.

6   IEEE JOURNAL OF SELECTED TOPICS IN APPLIED EARTH OBSERVATIONS AND REMOTE SENSING
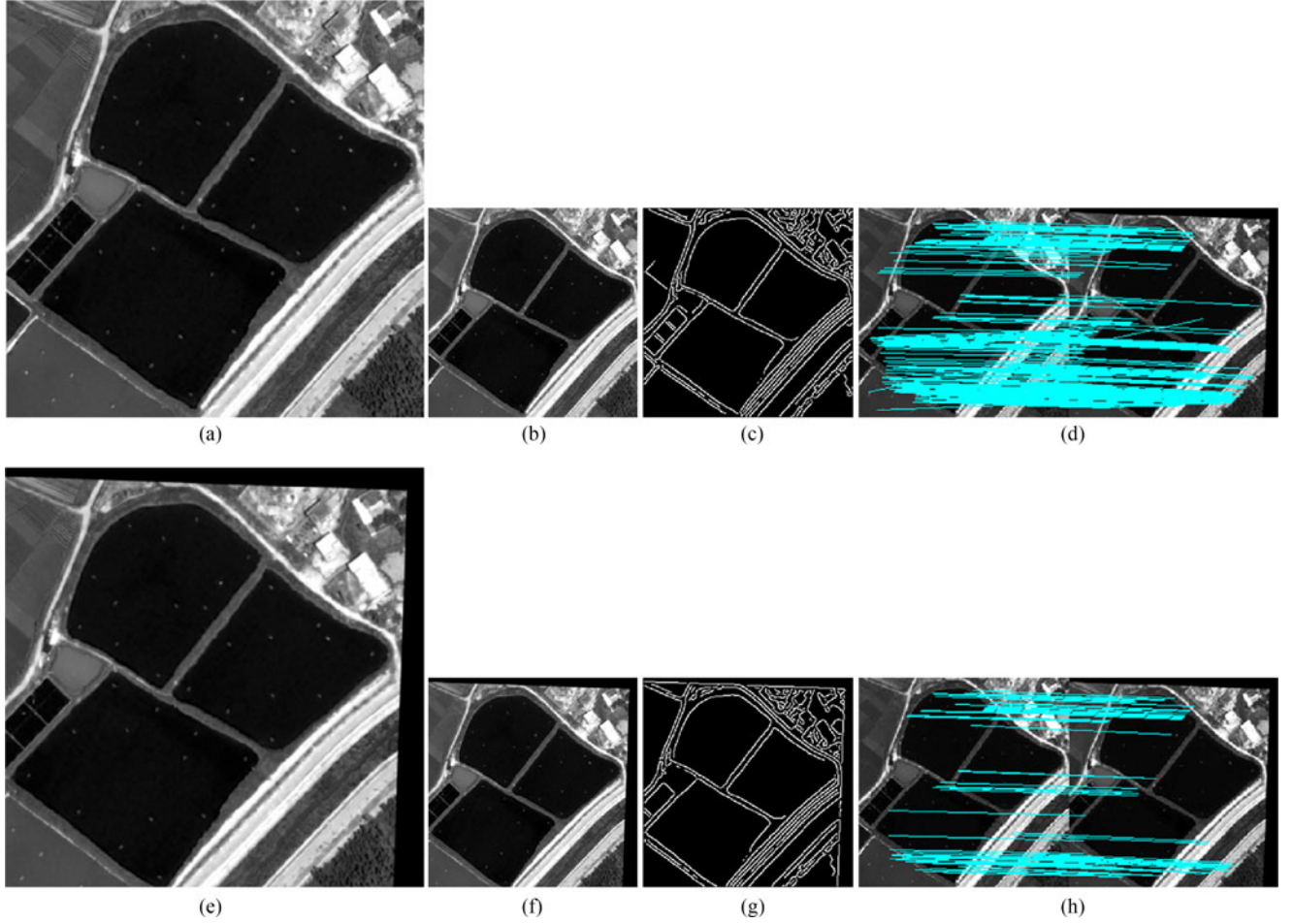
Fig. 4. WV-2 Pan image registration. (a) Reference image. (b) ARI after HWT. (c) ARI after Canny edge detection. (d) Initial MPPs based on the approximate image. (e) Sensed image. (f) ASI after HWT. (g) ASI after Canny edge detection. (h) Filtered MPPs after the variation RANSAC by adding the quality constraint.

registered image for automatic registration based SIFT, SURF, and AMEPF.

The experimental environment of all automatic registration is Intel Core I5, Quad-core processors, memory 8 GB, operating system windows 7, MATLAB 2014a.

For the assessment, the registration results are evaluated by using four quantitative evaluation indexes including the matching ratio (MR), the matching efficiency (ME), the root mean square error (RMSE), and the time consuming

$$\text{MR} = \frac{\text{Number of MPPs after RANSAC}}{\text{Number of initial MPPs}} \tag{7}$$

$$\text{ME} = \frac{\text{MR}}{\text{Time}} \tag{8}$$

$$\text{RMSE} = \sqrt{\frac{1}{k} \sum \left((x_p - x_q)^2 + (y_p - y_q)^2 \right)}. \tag{9}$$

Herein, $p \in [1, k]$, $q \in [1, k]$, k is the number of the selected MPPs, x_p, y_p are the coordinates of matching points in the registered image, x_q, y_q are the coordinates of corresponding matching points in the reference image, respectively. The smaller the RMSE is, the higher the accuracy of registration is.

When RMSE is less than 1, the registration precision reaches the subpixel level.

A. Same Sensor Optical Image Registration

Fig. 4 shows the reference image (WV-2 Pan band), the sensed image (the transformed WV-2 Pan band), the approximate images after HWT, and the canny edge extraction images. After the one-level HWT, the size of the approximate image is reduced to the half of the original image. Although some details are lost, edge features are still extracted well by the canny operator. In addition, the ARI and the ASI are adopted to extract the EPFs for matching. Thus, the registration speed can be improved by four times theoretically.

Fig. 4 also shows the MPPs before and after the variation RANSAC filtering based on the approximate images. As shown in Fig. 4(h), the error MPPs are almost all filtered out by the variation RANSAC filtering.

Fig. 5 shows the registration result and the superimposed image of the reference and registered images. Fig. 5(a) shows the registered image. Fig. 5(b) shows the superimposed image of the reference and registered images, which displays the registration effect in blocks to show whether the stitching line from block to

This article has been accepted for inclusion in a future issue of this journal. Content is final as presented, with the exception of pagination.

GUO *et al.*: HIGH-RESOLUTION REMOTE-SENSING IMAGE REGISTRATION BASED ON ANGLE MATCHING OF EDGE POINT FEATURES 7
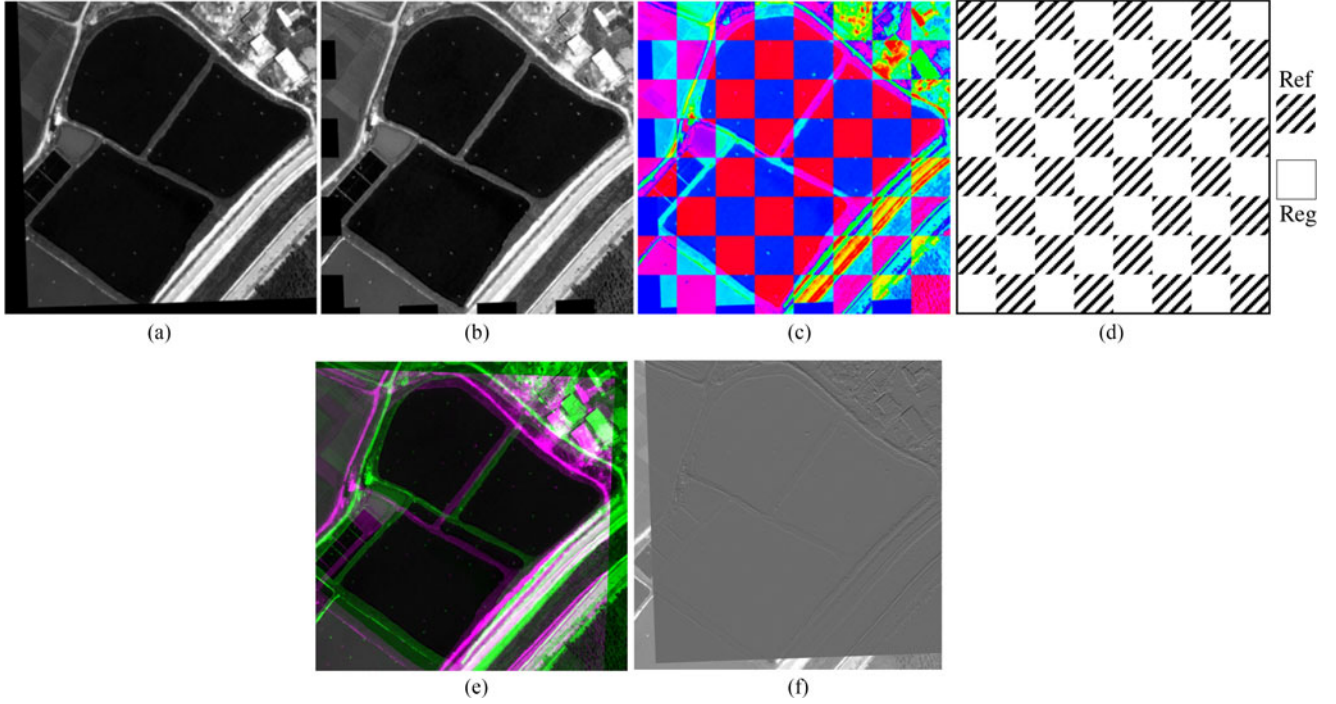

Fig. 5. Registration result of the same sensor optical WV-2 Pan image. (a) Registered image of AMEPF. (b) Superimposed image of the reference and the registered images in the block way. (c) Pseudocolor superimposed image in blocks. (d) Superimposition block order. (e) Combination of reference and sensed images before registration. (f) Difference image after AMEPF registration.

block is smooth. In order to show the registration superposition effect more clearly, the reference image and the registered image are first processed by pseudocolor processing [28], and then are superimposed in blocks by the same above way, as shown in Fig. 5(c). Fig. 5(d) shows the superimposition block order of the reference image and the registered image. Meanwhile, in order to more intuitively display the registration effect, the combination of the reference and sensed images before registration, and the difference of the reference and registered images after registration are shown in Fig. 5(e) and (f) [29], [30]. From Fig. 5(b) and (c), the reference image and the registered image are well spliced with smooth seams. Fig. 5(e) shows the evident dislocation before registration. From the difference image in Fig. 5(f), which corresponds to the errors in the registration process, the reference and sensed images are well registered with high accuracy.

Table II shows the registration result comparison of SIFT, SURF, manual, and AMEPF algorithms. From Table II, the SIFT algorithm has the most numbers of MPP after the original RANSAC, but the registration time is the longest and the ME is the lowest. Although the SURF algorithm has the fastest registration speed, the MR is the lowest and the RMSE is the largest. The proposed AMEPF method is higher than both SIFT and SURF algorithms in the MR and the registration accuracy. The proposed method also outperforms the manual registration. Since the time of manually selecting 30 control point pairs is subjective and is very long, only RMSE evaluation is considered for the manual registration.

In order to verify the correctness of theoretical speed enhancement after HWT, the EPF extraction and registration are processed from the original image and the approximate image, respectively. Table III shows the registration information of the WV-2 Pan band and the approximate image after HWT. Among them, the numbers of the EPFs extracted from the ARI, the ASI, the reference image, and the sensed image are 6318, 6104, 22 808, and 21 050, respectively. The MPPs of the ARI are 303 pairs, and the final are 74 pairs after the variation RANSAC filtering the mismatched or error pairs. The initial MPPs of the original images are 803 pairs, and the final are 71 pairs after the variation RANSAC filtering.

Table III also shows the comparison of the registration accuracy and time with and without HWT. The RMSEs are up to subpixel registration accuracy of both the approximate image and the original image. But, the registration time of the original image is far greater than the approximate image after HWT, which is nearly five times. The numbers of the extracted EPFs from the approximate images after HWT are reduced, which greatly reduces the matching calculation of EPFs and improves the registration speed.

Moreover, in order to analyze the impact of different decomposition levels of HWT, the two-level HWT decomposition is also performed before the EPF extraction. The numbers of MPPs before and after the variation RANSAC are 151 and 43, respectively. The registration speed is improved by 30 times, comparing to that of the original image. However, the registration accuracy does not meet the application requirement with RMSE 3.175, as shown in Table III. Therefore, the using of HWT is a balance thing. The purpose of using HWT is to increase the speed, which is of great significance for high-resolution remote-sensing image with large

This article has been accepted for inclusion in a future issue of this journal. Content is final as presented, with the exception of pagination.

8   IEEE JOURNAL OF SELECTED TOPICS IN APPLIED EARTH OBSERVATIONS AND REMOTE SENSING

TABLE II
REGISTRATION PERFORMANCE COMPARISON OF FOUR METHODS FOR THE SAME SENSOR OPTICAL WV-2 PAN IMAGE

Method	Image	Number of EPFs	Number of MPPs	Number of MPPs after RANSAC	MR/%	Time/s	ME/%	RMSE/Pixel
SIFT	Reference	3742	2343	309	13.2	12.245	1.1	0.8669
	Sensed	3383						
SURF	Reference	1167	293	35	11.9	4.067	2.9	0.9877
	Sensed	1140						
Manual	Reference	30	30	----	----	----	----	0.7495
	Sensed	30						
AMEPF	Reference	6318	303	74	24.4	10.463	2.3	0.6376
	Sensed	6104						

TABLE III
REGISTRATION INFORMATION COMPARISON BETWEEN THE WV-2 PAN ORIGINAL IMAGE AND THE APPROXIMATE IMAGE AFTER HWT

Image type	Number of EPFs	Number of MPPs	Number of MPPs after RANSAC	Time/s	RMSE/pixel
ARI (one-level)	6318	303	74	10.463	0.6376
ASI (one-level)	6104				
Original reference image	22808	803	71	51.223	0.4092
Original sensed image	21050				
ARI (two-level)	1824	151	43	1.7	3.1750
ASI (two-level)	1888				

image size. Meanwhile, the approximate image after HWT needs to remain the sufficient spatial structure information for edge feature detection to further ensure the registration accuracy. When one-level HWT is used, the speed is improved much, at the same time, the accuracy is similar as the original image. When two-level HWT is used, the speed is improved much but the accuracy is also reduced much. Hence, only the one-level HWT decomposition is used as the tradeoff in the following experiments.

B. Same Sensor SAR Image Registration

The reference image is TerraSAR image. The sensed image is obtained by rotating and translating the reference image, as shown in Fig. 6. The corresponding edge extraction results based on the approximation image after HWT are also shown in Fig. 6.

Different from the experiment 1, the speckle noise in SAR image needs to be removed by using the enhanced Frost filter. Then, the HWT is carried out. The EPFs are extracted by the ROA operator based on the approximate image after HWT.

Fig. 7 shows the registration result and the superimposed result of the registered and reference images. Fig. 7(b) and (c) are displayed in the same way as Fig. 5(b) and (c). From the superimposed image, the stitching region is smooth liking one image. The difference image in Fig. 7(d) shows that the registration result is satisfactory.

Table IV shows the registration performance comparison of three algorithms. The SURF algorithm has the fastest registration speed and the SIFT algorithm is the slowest. The proposed AMEPF method is not much different from the SURF algorithm in the registration speed, but it is much higher than both the SIFT and SURF algorithms in MR and ME. In the registration accuracy, the RMSE value of the proposed AMEPF method is 0.4825, which is lowest comparing with the registration-based manual, SIFT, and SURF.
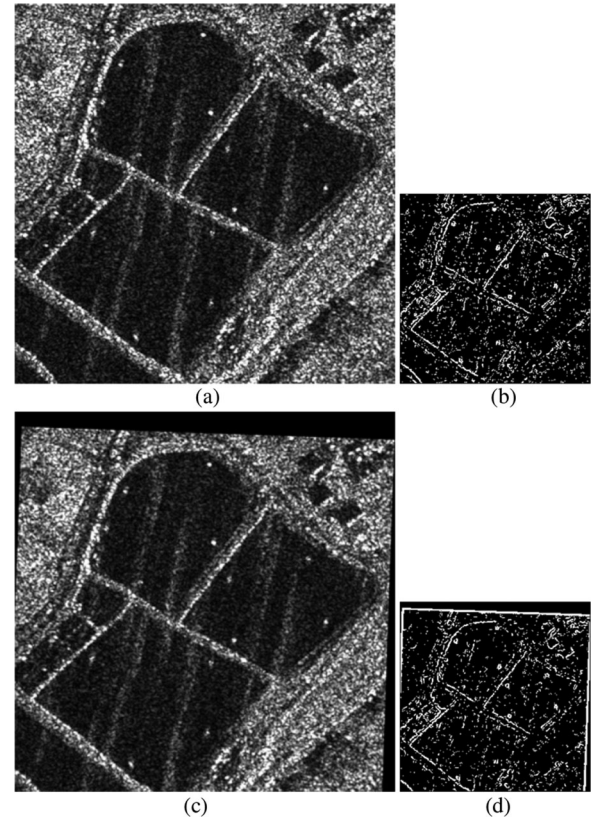

Fig. 6. Input images for TerraSAR image registration. (a) Reference image. (b) ARI after ROA edge detection. (c) Sensed image. (d) ASI after ROA edge detection.

C. Image Registration of Different Bands

Fig. 8 displays the reference image—the fifth band in WV-2 MS data, and the sensed image—the third band in WV-2 MS
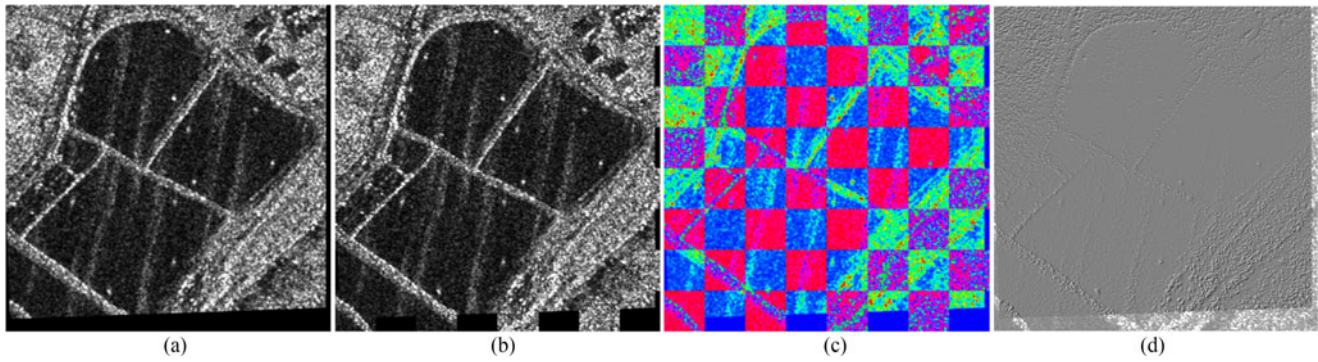
Fig. 7. Registration result of the same sensor TerraSAR image. (a) Registered image of AMEPF. (b) Superimposed image of the reference and registered images in blocks. (c) Pseudocolor superimposed image in blocks. (d) Difference image after AMEPF registration.

TABLE IV
REGISTRATION PERFORMANCE COMPARISON OF FOUR METHODS FOR THE SAME SENSOR TERRASAR IMAGE

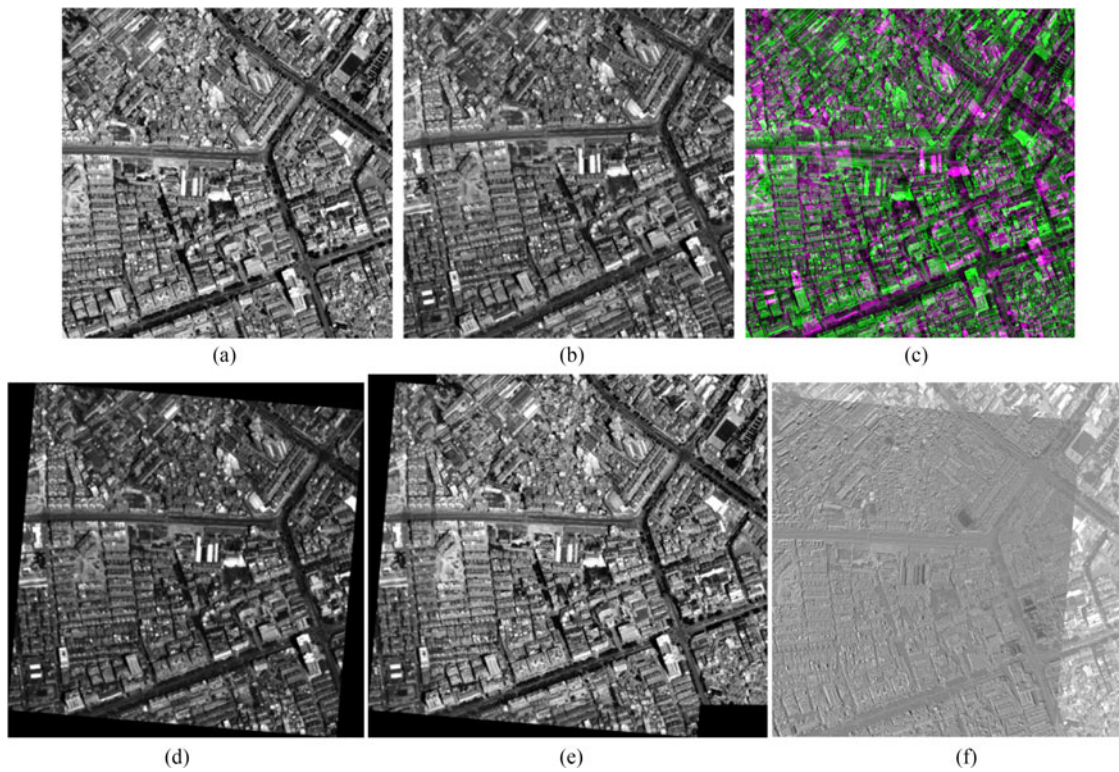| Method	Image	Number of EPFs	Number of MPPs	Number of MPPs after RANSAC	MR/%	Time/s	ME/%	RMSE/Pixel
SIFT	Reference	8222	5533	3686	66.6	18.397	3.6	0.6363
	Sensed	8262						
SURF	Reference	1312	423	197	46.6	5.422	8.5	0.7868
	Sensed	1242						
Manual	Reference	30	30	----	----	----	----	0.6130
	Sensed	30						
AMEPF	Reference	5583	1064	1035	97.3	7.552	12.9	0.4825
	Sensed	5168						

Fig. 8. Input images and the registration results of different WV-2 MS bands. (a) Reference image—the fifth MS band. (b) Sensed image—the third MS band. (c) Combination of reference and sensed images before registration. (d) Registered image of AMEPF. (e) Superimposed image of the reference and the registered images. (f) Difference image after AMEPF registration.

TABLE V
REGISTRATION PERFORMANCE COMPARISON OF FOUR METHODS FOR DIFFERENT WV-2 MS BANDS

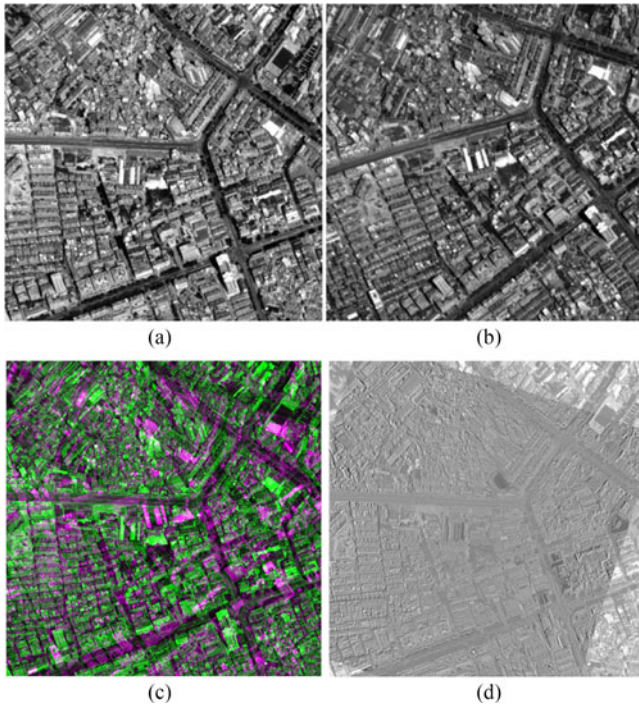| Method	Image	Number of EPFs	Number of MPPs	Number of MPPs after RANSAC	MR/%	Time/s	ME/%	RMSE/Pixel
SIFT	Reference Sensed	28417 24630	4125	4028	97.6	33.460	2.9	0.8994
SURF	Reference Sensed	1595 1590	327	125	38.2	7.876	4.9	1.2655
Manual	Reference Sensed	20 20	20	----	----	----	----	0.8226
AMEPF	Reference Sensed	14137 14029	105	50	47.6	19.080	2.5	0.3801

Fig. 9. Registration for different WV-2 MS bands after 18° rotation. (a) Reference image—the fifth MS band. (b) Sensed image—the third MS band after 18° rotation. (c) Combination of reference and sensed images before registration. (d) Difference image after AMEPF registration.
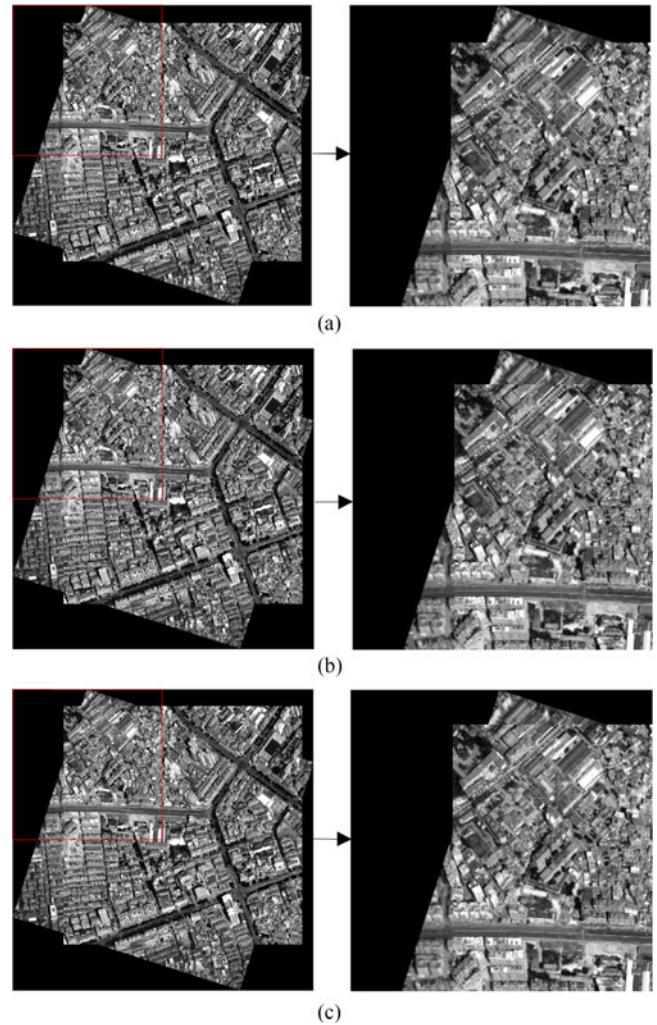

Fig. 10. Registration result for different WV-2 MS bands after 18° rotation. (a) Superimposed and enlarged partial images of AMEPF. (b) Superimposed and enlarged partial images of SIFT. (c) Superimposed and enlarged partial images of SURF.

data. The registration results are illustrated in Fig. 8(d) and (e). The registration effect is still exhibited by directly superimposing the reference image and the registered image. From Fig. 8(e), the texture and objects are very smooth and natural at the splice lines. From Fig. 8(c) and (f), the deformations before registration are rectified after registration.

Table V gives the registration performance comparison of different methods. The SIFT algorithm extracts 28 417 and 24 630 EPFs from the reference image and the sensed image, respectively. The SIFT finds 4125 MPPs and final 4028 pairs after the original RANSAC purification, which reduces 97 pairs. The SURF algorithm extracts 1595 and 1590 EPFs from the reference image and the sensed image, respectively. The SURF obtains 327 MPPs and final 125 pairs by reducing 202 pairs. The proposed AMEPF method extracts 14 137 and 14 029 EPFs from the ARI image and the ASI image, respectively. The AMEPF method obtains the final 50 MPPs after the variation RANSAC purification by reducing 55 pairs.

For the registration accuracy, the RMSE values of the AMEPF, manual, SURF, and SIFT are 0.3801, 0.8226, 1.2655, and 0.8994, respectively. It can be seen that the proposed AMEPF method is better than all the other methods in the case of MS image registration with different bands.

In order to prove the robustness against rotation of the proposed AMEPF method, the rotated image is used to do the registration. The original sensed image—the third band of

TABLE VI
REGISTRATION PERFORMANCE COMPARISON OF FOUR METHODS FOR DIFFERENT WV-2 MS BANDS AFTER 18° ROTATION

Method	Image	Number of EPFs	Number of MPPs	Number of MPPs after RANSAC	MR/%	Time/s	ME/%	RMSE/Pixel
SIFT	Reference	28417	1300	622	47.8	34.6	1.4	1.1798
	Sensed	23262						
SURF	Reference	1595	37	10	27.0	6.4	4.2	1.5916
	Sensed	1525						
Manual	Reference	10	10	----	----	----	----	0.9903
	Sensed	10						
AMEPF	Reference	14137	10	7	70.0	22.8	3.1	0.4899
	Sensed	14404						

WV-2 MS—is rotated 18° as the new sensed image. The reference image is still the fifth band of WV-2 MS, as shown in Fig. 9. The combination of the reference and sensed images before registration, the difference after registration are also shown in Fig. 9(c) and (d). The enlarged partial images of the registration results based on SIFT, SURF, and AMEPF are displayed in Fig. 10. As the enlarged partial images shown, the ground characteristics (roads and buildings) of the proposed AMEPF method are smooth and natural, but evident dislocations are existed in the SIFT and SURF methods.

Table VI exhibits the objective performance of the SIFT, SURF, and AMEPF methods. With the rotation angle increasing, the numbers of MPPs are decreased for all three registration methods. For the RMSE, the AMEPF method and the manual registration can achieve subpixel level, but SIFT and SURF methods gets more than one pixel.

D. Image Registration of Different Resolutions

The reference and the sensed images are WV-2 Pan band with 0.5-m resolution and the fifth MS WV-2 band with 2-m resolution, respectively (see Fig. 11). The overlapped image before registration and the difference image after registration are shown in Fig. 11(c) and (d), respectively. From the clear contrast effect, the AMEPF registration result is satisfactory. For the manual registration, the superimposed result of the reference and registered images, and two enlarged partial images are shown in Fig. 11(e), in which there are some dislocations.

The superimposed effect of the reference and registered images are displayed in Fig. 12. From Fig. 12(a), for the AMEPF method, the objects and textures are still natural in the stitching lines. However, for the SIFT and SURF results, as shown in Fig. 12(b) and (c), respectively, it is clear that the ground features have some dislocation phenomenon.

The objective evaluation of the registration performance is shown in Table VII. Although the resolution of the reference image is four times to that of the sensed image, a certain number of MPPs can still be detected. The initial and filtered MPPs in the AMEPF method are 122 and 115 pairs, respectively.

In Table VII, the time spent by the SIFT algorithm is 2.7 times that of the SURF algorithm, and is 1.5 times that of the proposed AMEPF algorithm. For the MR, the AMEPF method is the best, whereas the SIFT method is the second best and the SURF method is the lowest. In the aspect of ME, the SIFT and SURF algorithms are almost the same. The AMEPF method is 13.6%,
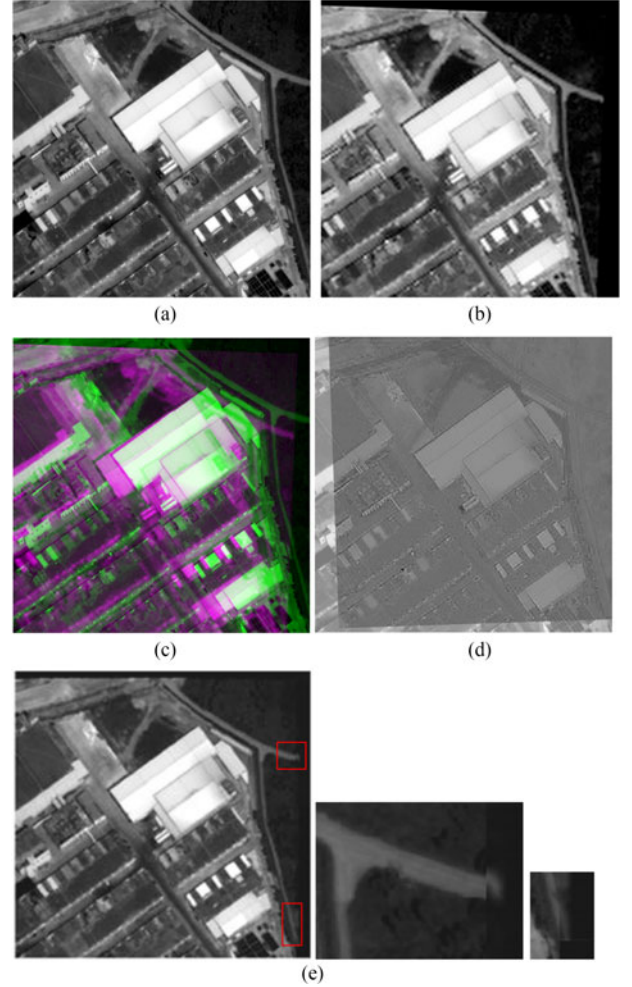

Fig. 11. Registration for different resolutions. (a) Reference image—the WV-2 Pan band. (b) Sensed image—the fifth WV-2 MS band. (c) Combination of reference and sensed image before registration. (d) Difference after AMEPF registration. (e) Superimposed and enlarged partial images of manual registration.

which is 1.7 times that of the SIFT and SURF algorithms. From the most important registration accuracy, the proposed AMEPF method is the best comparing to the manual, SIFT and SURF.

E. Image Registration of Different Temporal Sensors with Large Size

The reference and sensed images are WV-2 Pan (October 11, 2014) and Pleiades Pan images (November 14, 2016),

TABLE VII
REGISTRATION PERFORMANCE COMPARISON OF FOUR METHODS FOR WV-2 PAN AND MS IMAGES

Method	Image	Number of EPFs	Number of MPPs	Number of MPPs after RANSAC	MR/%	Time/s	ME/%	RMSE/Pixel
SIFT	Reference	3630	1656	1379	83.3	10.384	8.0	2.8471
	Sensed	5077						
SURF	Reference	1132	47	15	31.9	3.904	8.2	5.3557
	Sensed	1184						
Manual	Reference	20	20	----	----	----	----	1.7637
	Sensed	20						
AMEPF	Reference	7460	122	115	94.3	6.937	13.6	1.7423
	Sensed	6760						
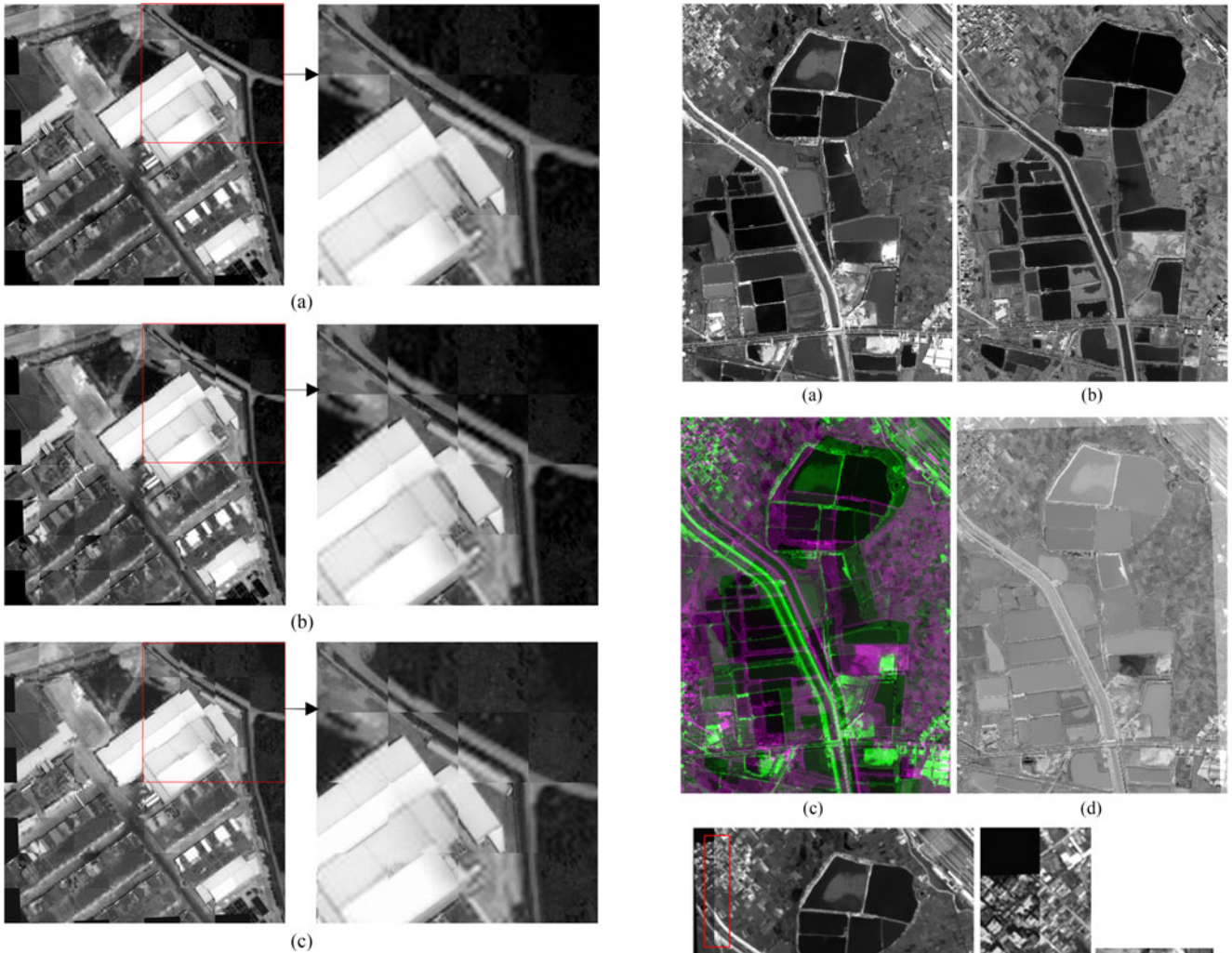
Fig. 12. Registration result for different resolutions of WV-2 images. (a) Superimposed and enlarged partial images of AMEPF. (b) Superimposed and enlarged partial images of SIFT. (c) Superimposed and enlarged partial images of SURF.

Fig. 13. Registration for WV-2 and Pleiades. (a) Reference image—the WV-2 Pan band. (b) Sensed image—the Pleiades Pan band. (c) Combination of reference and sensed images before registration. (d) Difference image after AMEPF registration. (e) Superimposed and enlarged partial images of manual registration.

respectively (see Fig. 13). The superposition of the reference and sensed images before registration, and the difference after AMEPF registration shown in Fig. 13(c) and (d) evidently display that the sensed image is well registered to the reference image. About the manual registration [see Fig. 13(e)], the superimposed image of the reference and registered images, and the enlarged partial images show that there are some dislocations in the stitching lines.

This article has been accepted for inclusion in a future issue of this journal. Content is final as presented, with the exception of pagination.

GUO *et al.*: HIGH-RESOLUTION REMOTE-SENSING IMAGE REGISTRATION BASED ON ANGLE MATCHING OF EDGE POINT FEATURES
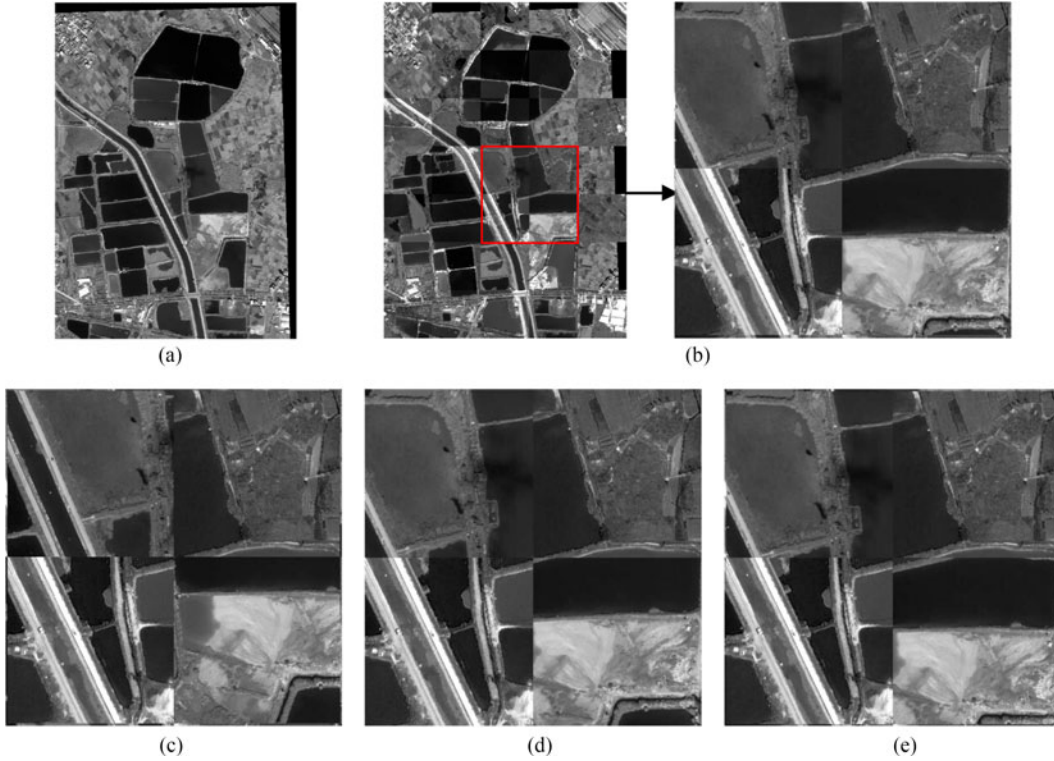
13

Fig. 14. Registration result of WV-2 and Pleiades images. (a) Registered image of AMEPF. (b) Superimposed and enlarged partial images of AMEPF. (c) Enlarged partial image before registration. (d) Enlarged partial image of SIFT. (e) Enlarged partial image of SURF.

TABLE VIII
REGISTRATION PERFORMANCE COMPARISON OF FOUR METHODS FOR WV-2 PAN AND PLEIADES PAN

Method	Image	Number of EPFs	Number of MPPs	Number of MPPs after RANSAC	MR/%	Time/s	ME/%	RMSE/Pixel
SIFT	Reference Sensed	155678 202627	779	58	7.4	2291.859	0.003	1.8450
SURF	Reference Sensed	31650 31095	106	31	29.2	466.417	0.06	4.0573
Manual	Reference Sensed	20 20	20	----	----	----	----	1.7669
AMEPF	Reference Sensed	97392 106443	40	28	70	965.404	0.07	0.5676

In order to better compare the registration results, this experiment gives the partial enlarged superimposed image of the WV-2 Pan and Pleiades Pan before registration [see Fig. 14(c)], which are with the obvious dislocations. In Fig. 14(b) of the AMEPF method, the ground characteristics and textures are connected naturally and smoothly in the stitching lines, although the reference image and the sensed image have different sensors and different time phases. However, the SIFT and SURF methods still have evident dislocations in the stitching lines, as shown in Fig. 14(d) and (e).

Table VIII gives the quantitative comparison of the registration performance for four methods. Although the SIFT algorithm detects the most EPFs and MPPs, it also contains the most error MPPs. Thus, the MR is only 7.4%. The proposed AMEPF method has more EPFs than that of SURF. Although the MPPs are less than those of SIFT and SURF, the error MPPs is the least in the three automatic methods. Moreover, both the MR and

ME values are the highest in the proposed AMEPF method. In the RMSE aspect, the AMEPF method is also lower than SIFT, SURF, and manual registration. Thus the registration accuracy of AMEPF is the best. Overall, comparing with the SIFT, SURF, and manual registration, this proposed AMEPF method has the best performance in large size high-resolution remote-sensing image registration for different temporal and sensors.

In summary, the proposed AMEPF method achieves the subpixel registration accuracy, except the registration of different resolutions with four times resolution difference. In all five high-resolution experiment situations, the accuracy of AMEPF is the highest, the manual registration is the second highest, then are the SIFT-based and SURF-based methods. The manual registration also obtains the subpixel accuracy except the last two experiments for different resolutions and different temporal sensors. However, the accuracy of the manual registration is mainly related to the selected control point pairs. But, it is not easy to

choose precise control point pairs. Moreover, the selecting process is subjective, time-consuming, and laborious. Especially, the more complex the remote-sensing images are, the less accurate it is to choose control point pairs. Hence, for the complex images (for example, the last two experiment situations in Tables VII and VIII), it is even hard to select optimal control point pairs.

IV. CONCLUSION

In this paper, an automatic feature-level registration method for high-resolution remote-sensing images is proposed to improve the processing speed and the registration accuracy. The HWT is applied to reduce the image size while preserving the main structure of the image, which improves the registration speed. The EPF is considered because of its accurate positioning and stable features. In the feature matching, angle ratios between the vectors of EPFs are calculated and multiple directions for one EPF are set to enhance the registration accuracy and the robustness. During the MPPs filtering, the original RANSAC is changed by adding the constraint condition of feature point pair quality, in order to improve the accuracy and the speed of image registration.

Moreover, in the aspect of the affine transform parameter calculation, the MPPs are selected uniformly by blocks to improve the registration accuracy. Five kinds of experiments are performed to verify the effectiveness of the proposed AMEPF registration method, such as, the same sensor optical registration, the same sensor SAR registration, registration of different bands, registration of different resolutions, and registration of different temporal and sensors with large size for high-resolution remote-sensing images. The SIFT-based, SURF-based, and manual registration methods are compared. The registration results are evaluated quantitatively by using four objective indexes including the matching ratio, the matching efficiency, the RMSE, and the time consuming. Five types of experimental results demonstrate the effectiveness, reliability, and applicability of the proposed AMEPF method. The registration accuracy in different experimental conditions can achieve subpixel level, even in large size with 2000×2800 and even in rotation angle with $18°$. In the future, the registration of optical and SAR images will be considered in the subsequent research work.

REFERENCES

[1] Q. Zhang, Z. G. Cao, Z. W. Hu, Y. H. Jia, and X. L. Wu, "Joint image registration and fusion for panchromatic and multispectral images," *IEEE Geosci. Remote Sens. Lett.*, vol. 12, no. 3, pp. 467–471, Mar. 2015, doi: 10.1109/LGRS.2014.2346398.

[2] B. Zitová and J. Flusser, "Image registration methods: A survey," *Image Vis. Comput.*, vol. 21, no. 11, pp. 977–1000, 2003, doi: 10.1016/S0262-8856(03)00137-9.

[3] J. Y. Li, Q. W. Hu, and M. Y. Ai, "Robust feature matching for remote sensing image registration based on lq-estimator," *IEEE Geosci. Remote Sens. Lett.*, vol. 13, no. 12, pp. 1989–1993, Dec. 2016, doi: 10.1109/LGRS.2016.2620147.

[4] A. Sedaghat and H. Ebadi, "Distinctive order based self-similarity descriptor for multi-sensor remote sensing image matching," *ISPRS J. Photogramm. Remote Sens.*, vol. 108, pp. 62–71, 2015, doi: 10.1016/j.isprsjprs.2015.06.003.

[5] A. Sedaghat and H. Ebadi, "Remote sensing image matching based on adaptive binning sift descriptor," *IEEE Trans. Geosci. Remote Sens.*, vol. 53, no. 10, pp. 5283–5293, Oct. 2015, doi: 10.1109/TGRS.2015.2420659.

[6] Y. Ke and R. Sukthanka, "PCA-SIFT: A more distinctive representation for local image descriptors," in *Proc. IEEE Comput. Soc. Conf. Comput. Vis. Pattern Recognit.*, 2004, pp. 506–513, doi: 10.1109/CVPR.2004.1315206.

[7] B. Kupfer, N. Netanyahu, and I. Shimshoni, "An efficient sift-based mode-seeking algorithm for sub-pixel registration of remotely sensed images," *IEEE Geosci. Remote Sensing Lett.*, vol. 12, no. 2, pp. 379–383, Feb. 2015, doi: 10.1109/LGRS.2014.2343471.

[8] J. Y. Ma, H. B. Zhou, J. Zhao, and J. W. Tian, "Robust feature matching for remote sensing image registration via locally linear transforming," *IEEE Trans. Geosci. Remote Sens.*, vol. 53, no. 12, pp. 6469–6481, Dec. 2015, doi: 10.1109/TGRS.2015.2441954.

[9] C. Zhao and A. A. Goshtasby, "Registration of multitemporal aerial optical images using line features," *ISPRS J. Photogramm. Remote Sens.*, vol. 117, pp. 149–160, 2016, doi: 10.1016/j.isprsjprs.2016.04.002.

[10] F. Q. Liu, F. K. Bi, L. Chen, and W. Liu, "Feature-area optimization: a novel SAR image registration method," *IEEE Geosci. Remote Sens. Lett.*, vol. 13, no. 2, pp. 242–246, Feb. 2016, doi: 10.1109/LGRS.2015.2507982.

[11] N. Merkle, R. Müller, P. Schwind, G. Palubinskas, and P. Reinartz, "A new approach for optical and sar satellite image registration," *ISPRS Ann. Photogramm., Remote Sens. Spatial Inf. Sci.*, vol. II-3/W4, pp. 119–126, 2015, doi: 10.5194/isprsannals-II-3-W4-119-2015.

[12] S. Nagarajan and T. Schenk, "Feature-based registration of historical aerial images by area minimization," *ISPRS J. Photogramm. Remote Sens.*, vol. 116, pp. 15–23, 2016, doi: 10.1016/j.isprsjprs.2016.02.012.

[13] X. M. Li, L. Zheng, and Z. Y. Hu, "SIFT based automatic registration of remotely-sensed imagery," *J. Remote Sens.*, vol. 10, no. 6, pp. 885–892, 2006.

[14] J. M. Murphy, J. L. Moigne, and D. J. Harding, "Automatic image registration of multimodal remotely sensed data with global shearlet features," *IEEE Trans. Geosci. Remote Sens.*, vol. 54, no. 3, pp. 1685–1704, Mar. 2016, doi: 10.1109/TGRS.2015.2487457.

[15] S. Paul and U. C. Pati, "Remote sensing optical image registration using modified uniform robust SIFT," *IEEE Geosci. Remote Sens. Lett.*, vol. 13, no. 9, pp. 1300–1304, Sep. 2016, doi: 10.1109/LGRS.2016.2582528.

[16] L. Huang, C. Chen, H. Shen, and B. He, "Adaptive registration algorithm of color images based on SURF," *Measurement*, vol. 66, pp. 118–124, 2015, doi: 10.1016/j.measurement.2015.01.011.

[17] D. G. Lowe, "Object recognition from local scale invariant features," in *Proc. 7th IEEE Int. Conf. Comput. Vis.*, Corfu, Greece, 1999, pp. 1150–1157, doi: 10.1109/ICCV.1999.790410.

[18] D. G. Lowe, "Distinctive image features from scale invariant key points," *Int. J. Comput. Vis.*, vol. 60, no. 2, pp. 91–110, 2004, doi: 10.1023/B:VISI.0000029664.99615.94.

[19] O. U. Pramote and P. Piamsa-Nga, "Improve accuracy of disparity map for stereo images using SIFT and weighted color model," in *Proc. 7th Int. Conf. Knowl. Smart Technol.*, Chonburi, Thailand, 2015, pp. 109–114, doi: 10.1109/KST.2015.7051470.

[20] H. Bay, A. Ess, T. Tuytelaars, and L. V. Gool, "Speeded-up robust features (SURF)," *Comput. Vis. Image Understanding*, vol. 110, no. 3, pp. 346–359, 2008, doi: 10.1016/j.cviu.2007.09.014.

[21] F. H. Huang, Z. Y. Mao, and W. Z. Shi, "ICA-ASIFT-based multi-temporal matching of high-resolution remote sensing urban images," *Cybern. Inf. Technol.*, vol. 16, no. 5, pp. 34–49, 2016, doi: 10.1515/cait-2016-0050.

[22] S. W. Xiang, G. J. Wen, F. Gao, and Y. J. Wu, "High resolution remote sensing image registration method based on multi-model representation," *Transducer Microsyst. Technol.*, vol. 34, no. 10, pp. 22–24, 2015, doi: 10.13873 /J.1000-9787(2015)10-0022-03.

[23] J. Canny, "A computational approach to edge detection," *IEEE Trans. Pattern Anal. Mach. Intell.*, vol. PAMI-8, no. 6, pp. 679–698, Nov. 1986, doi: 10.1109/TPAMI.1986.4767851.

[24] R. Touzi, A. Lopes, and P. Bousquet, "A statistical and geometrical edge detector for SAR images," *IEEE Trans. Geosci. Remote Sens.*, vol. 26, no. 6, pp. 764–773, Nov. 1988, doi: 10.1109/36.7708.

[25] W. B. Rong, Z. J. Li, W. Zhang, and L. N. Sun, "An improved canny edge detection algorithm," in *Proc. IEEE Int. Conf. Mechatronics Automat.*, Tianjin, China, 2014, pp. 577–582, doi: 10.1109/ICMA.2014.6885761.

[26] M. A. Fischler and R. C. Bolles, "Random sample consensus: a paradigm for model fitting with applications to image analysis and automated cartography," *Commun. ACM*, vol. 24, no. 6, pp. 381–395, 1981, doi: 10.1145/358669.358692.

[27] R. Hartley and A. Zisserman, *Multiple View Geometry in Computer Vision*. Cambridge, U.K.: Cambridge Univ. Press, 2003, pp. 281–282.

[28] T. F. Cai, F. Zhu, Y. M. Hao, and H. J. Fan, "Pseudo-color processing of gray images for human visual detection and recognition," *Infrared Laser Eng.*, vol. 44, no. S, pp. 213–219, 2015, doi: 10.3969/j.issn.1007-2276.2015.z1.039.

[29] S. M. M. Kahaki, M. J. Nordin, A. H. Ashtari, and S. J. Zahra, "Deformaiton invariant image matching based on dissimilarity of spatial features," *Neurocomputing*, vol. 175, pp. 1009–1018, 2016, doi: 10.1016/j.neucom.2015.09.106.

[30] S. M. M. Kahaki, M. J. Nordin, A. H. Ashtari, and S. J. Zahra, "Invariant feature matching for image registration application based on new dissimilarity for spatial features," *PLoS ONE*, vol. 11, no. 3, 2016, Art. no. e0149710, doi: 10.1371/journal.pone.0149710.

Mengmeng He received the B.S. degree in geographic information system from Shanghai Normal University, Shanghai, China, in 2014, and the M.S. degree in signal and information processing from the Institute of Remote Sensing and Digital Earth, Chinese Academy of Sciences, Beijing, China, and the University of Chinese Academy of Sciences, Beijing, China, in 2017.

She is currently with the Jiuzhou Hongtu Technology Company, Ltd., Beijing, China, and the Beijing Institute of Surveying and Mapping, Beijing, China. Her research interests include remote-sensing image processing.

Qing Guo (M'09) received the M.Sc. and Ph.D. degrees in optics from the Harbin Institute of Technology, Harbin, China, in 2006 and 2010, respectively.

She joined the Institute of Remote Sensing and Digital Earth, Chinese Academy of Sciences, Beijing, China, in 2010, where she is currently an Associate Professor. From 2007 to 2009, she was an exchange Ph.D. student in the Department of Electrical and Computer Engineering, University of Calgary, Calgary, AB, Canada. From 2014 to 2015, she was a Visiting Scholar with the Institute for Geoinformatics and Remote Sensing, University of Osnabrück, Osnabrück, Germany. Her research interests include remote-sensing information extraction and processing, including the image registration and fusion, and her other research interests include information security, image encryption, and digital watermarking.

An Li received the B.S. degree in electronic engineering from Tsinghua University, Beijing, China, in 1989, and the M.S. degree in computer application from the Graduate University of Chinese Academy of Sciences, Beijing, China, in 1992.

He is currently the Director of the China Remote Sensing Satellite Ground Station (RSGS), Institute of Remote Sensing and Digital Earth, Chinese Academy of Sciences, Beijing, China. He joined the RSGS in 1992 and worked in the remote-sensing data processing for the following years. He is currently in charge of the management of the satellite ground segment operation and engineering.